

FORS spectroscopy of galaxies in the Hubble Deep Field-South

Dimitra Rigopoulou^{1,2*}, William D. Vacca^{3,2}, Stefano Berta⁴,
Alberto Franceschini⁴, and Hervé Aussel⁵

¹ Astrophysics, University of Oxford, Keble Rd, Oxford, OX1 3RH, U.K.

² Max-Planck-Institut für extraterrestrische Physik (MPE), Postfach 1312, Garching D-85741, Germany

³ USRA, NASA Ames Research Center, MS 144-2 Moffett Field, CA 94035-1000 USA

⁴ Dipartimento di Astronomia, Università di Padova, Vicolo dell'Osservatorio 2, I-35122, Padova, Italy

⁵ Institute for Astronomy, 2680 Woodlawn Drive, Honolulu, Hawaii, 96822, USA

Abstract. We present low resolution multi-object spectroscopy of an I-band magnitude limited ($I_{AB} \simeq 23\text{--}23.5$) sample of galaxies located in an area centered on the Hubble Deep Field-South (HDFS). The observations were obtained using the Focal Reducer/low dispersion Spectrograph (FORS) on the ESO Very Large Telescope. Thirty-two primary spectroscopic targets in the HST-WFPC2 HDFS were supplemented with galaxies detected in the Infrared Space Observatory's survey of the HDFS and the ESO Imaging Deep Survey to comprise a sample of 100 galaxies for spectroscopic observations. Based on detections of several emission lines, such as [OII] $\lambda 3727$, H_{β} and [OIII] $\lambda 5007$, or of other spectroscopic features, we measured accurate redshifts for 50 objects in the central HDFS and flanking fields. The redshift range of the current sample of galaxies is 0.6–1.2, with a median redshift of 1.13 (at $I \simeq 23.5$ not corrected for completeness). The sample is dominated by starburst galaxies with only a small fraction of ellipticals ($\sim 10\%$). For the emission line objects, the extinction corrected [OII] $\lambda 3727$ line strengths yield estimates of star formation rates in the range 0.5–30 M_{\odot}/yr . We used the present data to derive the [OII] $\lambda 3727$ luminosity function up to redshift of 1.2. When combined with [OII] $\lambda 3727$ luminosity densities for the local and high redshift Universe, our results confirm the steep rise in the star formation rate (SFR) to $z \simeq 1.3$.

Key words. Cosmology: observations, surveys – Galaxies: luminosity function, mass function – Galaxies: starburst

1. Introduction

The Hubble Deep Field-South (HDFS, Williams et al. 2000, Casertano et al. 2000) has been the subject of extensive follow-up ground-based imaging observations at optical (ESO-Imaging Survey (EIS), DaCosta et al. 1998; Big Throughput Camera (BTC) survey, Teplitz et al. 2001), near-infrared (e.g DaCosta et al. 1998, Vanzella et al. 2001, Rudnick et al. 2001, Saracco et al., 2001) and mid-infrared (Infrared Space Observatory (ISO): Oliver et al. 2002; Mann et al. 2002; Aussel et al. 2005, in prep.) wavelengths. The field has also been observed by the Spitzer Telescope (Huang et al., 2005, in prep). The unprecedented spatial resolution and depth of the Hubble Space Telescope (HST) images have allowed a reliable morphological classification of objects in the field (e.g. the SUNY collaboration, available at <http://www.ess.sunysb.edu/astro/hdfs/wfpc2/wfpc2.html>). In addition, many groups (e.g. Vanzella et al. 2001, Rudnick et al. 2001) have used various techniques to estimate photometric redshifts for large samples of galaxies detected in the HDFS region. With such a wealth of imaging observations already in place, a systematic

spectroscopic follow-up of objects detected in the HDFS is imperative in order to fully exploit the data. To date, only a limited number of redshifts have been determined for selected objects in the HDFS: Lyman break galaxy candidates by Cristiani et al. 2000 and Vanzella et al. 2002; ISO-detected objects by Rigopoulou et al. 2000 and Franceschini et al. 2003; objects in the vicinity of the quasar J2233-606 by Tresse et al. 1999 and Bergeron et al. 1999. Recently, Vanzella et al. (2002) reported on low resolution spectroscopy of a sample of 65 galaxies from the HDFS targetting primarily high-redshift ($z > 2$) candidates while Sawicki & Mallen-Ornellas (2003) targeted lower redshift objects.

In this paper, we report on the optical spectroscopy of 100 objects located in the HDFS and flanking fields. We have determined accurate redshifts for 50 objects. The sample selection, observations and data reduction are explained in Section 2. The redshifts and redshift distribution are given in Section 3 while star formation rates and extinction estimates are discussed in Section 4. Finally, in Section 5 the [OII] $\lambda 3727$ luminosity function and the global star formation rate densities are presented. Throughout the paper we use $H_0 = 70 \text{ km s}^{-1} \text{ Mpc}^{-3}$, $q_0 = 0.5$ unless otherwise stated.

* dar@astro.ox.ac.uk

2. Sample Selection, Observations, and Data Reduction

The WFPC2 observations of the HDFS resulted in the detection of a number of objects down to a limiting magnitude $F814W_{AB} \sim 28$ mag (Casertano et al. 2000). From this sample, galaxies were selected with $F814W_{AB} = 23.7$ (corresponding to $I_{Vega} = 23$ mag), a limit imposed by the sensitivity of the FORS1 150I grism. This criterion resulted in a primary sample of 32 objects all within the central WFPC2 field. The primary sample was supplemented with objects from the Flanking Fields, all of which have identifications in the ESO Deep Imaging Survey (EIS) and the BTC catalog. Additionally we included objects selected from the ISO HDFS detections (Aussel et al. 2005, in prep). In all, our final sample included 100 objects.

The spectroscopic observations were carried out as part of ESO program ID 65.O-0418(A) from August 24-28, 2000, using the Focal Reducer Spectrograph (FORS1) (Appenzeller 2000), in the Multi-Object-Spectroscopy (MOS) mode, on the ANTU-ESO telescope (formerly UT1), on Paranal, Chile. The data presented here have been retrieved from ESO’s VLT science archive.

In the FORS1/MOS mode, 19 slits are placed on a mask covering a field of view (FOV) of 6.8×6.8 sq. arcmin. To cover the 30 primary objects 5 MOS settings were needed. The supplemental objects were observed in the slits that were not occupied by the primary targets in each MOS setting. The slits were 1.2 wide and 22.5 arcsec long. In most cases the target galaxy was placed in the middle of the slit, so as to enable proper background subtraction. In a few cases a second galaxy happened to fall in the same slit. Spectra of these serendipitous galaxies were also analysed. The *GRIS-300V*, and *GRIS-150I* grisms were used, covering the 4450-8650 Å and 6000-11000 Å ranges, respectively. The choice of grism was based on previous photometric redshift estimates for sample galaxies; for galaxies with $z_{phot} < 0.7$ the *GRIS-300V* grism was used, while the *GRIS-150I* grism was used for those galaxies with $z_{phot} > 0.7$. The pixel scale was 0.2 arcsec/pixel while the resolution was $\lambda/\Delta\lambda = 440$ and 260 for the *GRIS-300V* and *GRIS-150I* grisms, respectively. At each MOS position, three exposures of 1900 s each were obtained, for a total integration time of 5700 s per position. The seeing during acquisition of the spectra varied between 0.8-1.5 arcsec. In Table 1 we present details of the observations.

For each field there were 3 separate exposures which were co-added before spectral extraction. We reduced the MOS spectra by treating each of the 19 slits separately and using standard IRAF¹ routines. The individual spectra were bias-subtracted and flat-fielded in the standard manner. To remove the background sky emission we fit a low-order polynomial in the spatial direction at each col-

Table 1. Log of the FORS1/MOS Observations

Field	RA(J2000)	Dec(J2000)	Grism	Filter	$\lambda/\Delta\lambda$	t_{exp} (sec)
M 2	22:32:54.5	-60:33:45.9	300V	GG435	440	5700
M 4	22:33:12.0	-60:32:35.7	300V	GG435	440	5700
M 5	22:32:43.9	-60:33:24.7	150I	GG435	260	5700
M 9	22:32:39.4	-60:33:57.0	150I	OG590	260	5700
M 10	22:32:59.6	-60:34:18.1	150I	GG435	260	5700

umn and then subtracted it for each individual exposure. Most of the cosmic ray hits in the sky region of the spectral images were excluded from the fits with a sigma-rejection algorithm. We then extracted a variance-weighted one-dimensional spectrum. The final spectrum was wavelength calibrated using arc lamp spectra and flux-calibrated using the spectro-photometric standard stars included in the MOS frame. The spectra of the standard stars were reduced in the same way as the galaxy spectra.

In Table 2 we present an inventory of all objects targeted with FORS1/MOS. We list galaxy number, coordinates (in those cases where two galaxies are included in the slit we report only the position of the sample galaxy) and optical (UBVRI) and near-infrared (JHK) photometry. We give AB magnitudes, taken mostly from EIS but supplemented with data from the BTC survey available from <http://hires.gsfc.nasa.gov/research/hdfs-btc>. Additionally, we list HST identifications from the HDFS-WFPC2 catalogue (available from <http://archive.stsci.edu/pub/hdf-south/version2>) and the HDFS WFPC2 flanking fields catalogue (available from <http://archive.stsci.edu/pub/hdf-south/version1>). Finally, we also give ISO identifications (from Aussel et al., 2004 in prep).

HERE, TABLE 2 TO BE INSERTED

3. Results

3.1. Spectroscopic measures

In Figures 1a-1f and 2a-2b we show the final wavelength- and flux-calibrated spectra for each object in the M2, M4, M5, M10 (Figs. 1a-1f) and M9 fields (Figs. 2a-2b). The spectra have been grouped in the two figures according to the wavelength coverage: spectra in Figure 1 cover the 4450 to 8200 Å range (corresponding to the *GRIS-300V* grism) while those in Figure 2 cover the 6000-9200 Å range (corresponding to the *GRIS-150I* grism). Redshifts were determined based on the wavelengths of the detected emission lines (usually the [OII]λ3727 line

¹ IRAF is distributed by the National Optical Astronomy Observatories, which are operated by the Association of Universities for Research in Astronomy, Inc. under the cooperative agreement with the National Science Foundation.

originating in a starburst) or, in a few cases, absorption features such as the CaII H, K features (at 3968.5 and 3933.7 Å) prominent in the spectra of elliptical galaxies. When multiple emission lines were detected, we averaged the redshifts from these lines. In the cases where we detect absorption features we have not attempted to measure any properties of the feature. The shape of the underlying continuum (especially in cases where emission lines were present) was also taken into account and helped to constrain the redshifts more efficiently. In each spectrum we report the galaxy number (from Table 2) and the corresponding redshift and mark the position of both detected and expected emission/absorption lines. Note that emission features are not always seen at the expected locations of some lines (e.g., H β or [OIII] λ 5007). In several spectra there are residual [O I] night-sky lines at $\lambda\lambda$ 5577 and 6300-6364 that can sometimes lead to “spurious” emission features in the spectra. These lines are highly variable and could not always be properly removed during the sky subtraction step.

In total we have obtained spectra for 100 objects. Some of the objects were determined to be stars. We have detected continuum in 78 objects and measured redshifts in 50 of them. We supplemented our redshift estimates with additional values taken from the literature (Rigopoulou et al. 2000 and Franceschini et al. 2003).

In Table 3 we give the redshifts and the emission line fluxes measured from the present spectra. In the majority of the spectra we detect [OII] λ 3727 and in some cases the [OIII] λ 4958 and λ 5007 lines as well. In half a dozen galaxies we measured H β λ 4861 line fluxes. Our measured redshifts are in agreement with the redshifts of Sawicki and Mallen Ornellas (2003), although the two lists are complementary as these authors target lower redshift objects. Although we did not perform a detailed classification of objects based on their spectral properties, it is evident that the majority of the sample seem to be starburst galaxies in the redshift range $z=0.6-1.2$. We detected only a small fraction (less than 10%) of elliptical galaxies². The highest redshift object in our sample (no. 48) is a QSO at $z=1.561$. Because of its redshift the Balmer lines are redshifted into the near-infrared regime; in our optical spectra we detected C III] λ 1909 and MgII λ 2798 Å. There is very good agreement between the redshift determined from the present optical spectra and the near-infrared spectra of Franceschini et al. (2003). Redshifts for objects nos. 37 and 89 in our sample were determined independently from near-infrared data as well, and the agreement with our estimates is quite good. Based on the measured [OII] λ 3727 line fluxes we have calculated the individual expected SFR([OII] λ 3727) (see Section 4 for details). We note that the spectral profiles were examined carefully in order to exclude objects displaying broad lines (ie containing type 1 Seyferts and QSOs) from the further

estimates of the luminosity function (LF) and the total SFR density (see section 5.1, 5.2).

HERE, TABLE 3 TO BE INSERTED

3.2. Median Redshift

We estimated the median redshift as a function of the I_{AB} magnitude using the values given in Table 2. A plot of the median redshift vs. I_{AB} magnitude is presented in Figure 3. For the plot we have used the entire FORS sample, i.e. objects from the main WFPC2 area, the Flanking Fields and the ISO selected targets (see Table 2). Although we have determined redshifts for the majority of the objects, the sample is rather incomplete at the fainter magnitudes. Assuming that $n_i(z)$ and $n_i(tot)$ are, respectively, the number of galaxies with spectroscopic redshift and the total number of galaxies (down to $I\sim 23.5$), then the completeness function in a given magnitude interval is defined as:

$$\eta_i = n_i(z)/n_i(tot) \quad (1)$$

In estimating the completeness function (Eqn. 1) we assumed that there are no biases or systematic effects and that the measured redshifts provide a fair sample of all possible redshifts in each bin. We then correct for the incompleteness by dividing the number of galaxies in each bin by η_i . In Figure 3 we plotted the galaxy redshift as a function of I_{AB} magnitude for the entire FORS sample. We find that a median redshift of 1.16 is reached by $I_{AB} \sim 23.5$ (corrected for incompleteness).

Finally, Figure 4 shows the redshift distribution for our spectroscopic sample. The distribution shows an evident peak at $z\sim 0.58$ which is most likely due to the large scale structure present in the HDF-S region (e.g. Arnouts et al. 2002, Vanzella et al. 2002).

4. Extinction and SFR estimates

For ionization-bounded HII regions the Balmer emission line luminosities scale directly with the ionizing luminosities of the exciting stars and thus are proportional to the star formation rate (SFR). Therefore, it is possible to use the Balmer emission lines to derive SFR in each galaxy. Traditionally, H α has been used to estimate SFR in galaxies in the redshift range up to $z\sim 0.4$; beyond this redshift, H α moves out of the optical window and can be accessed at $z>0.8$ in the near-infrared regime. At redshifts $0.5<z<1.4$, the [OII] λ 3727 emission line can be used to study the star formation rates.

The conversion factor between [OII] luminosity and SFR is computed using an evolutionary synthesis model.

² We labeled as “ellipticals” those galaxies whose spectra show the absorption CaII H, K features.

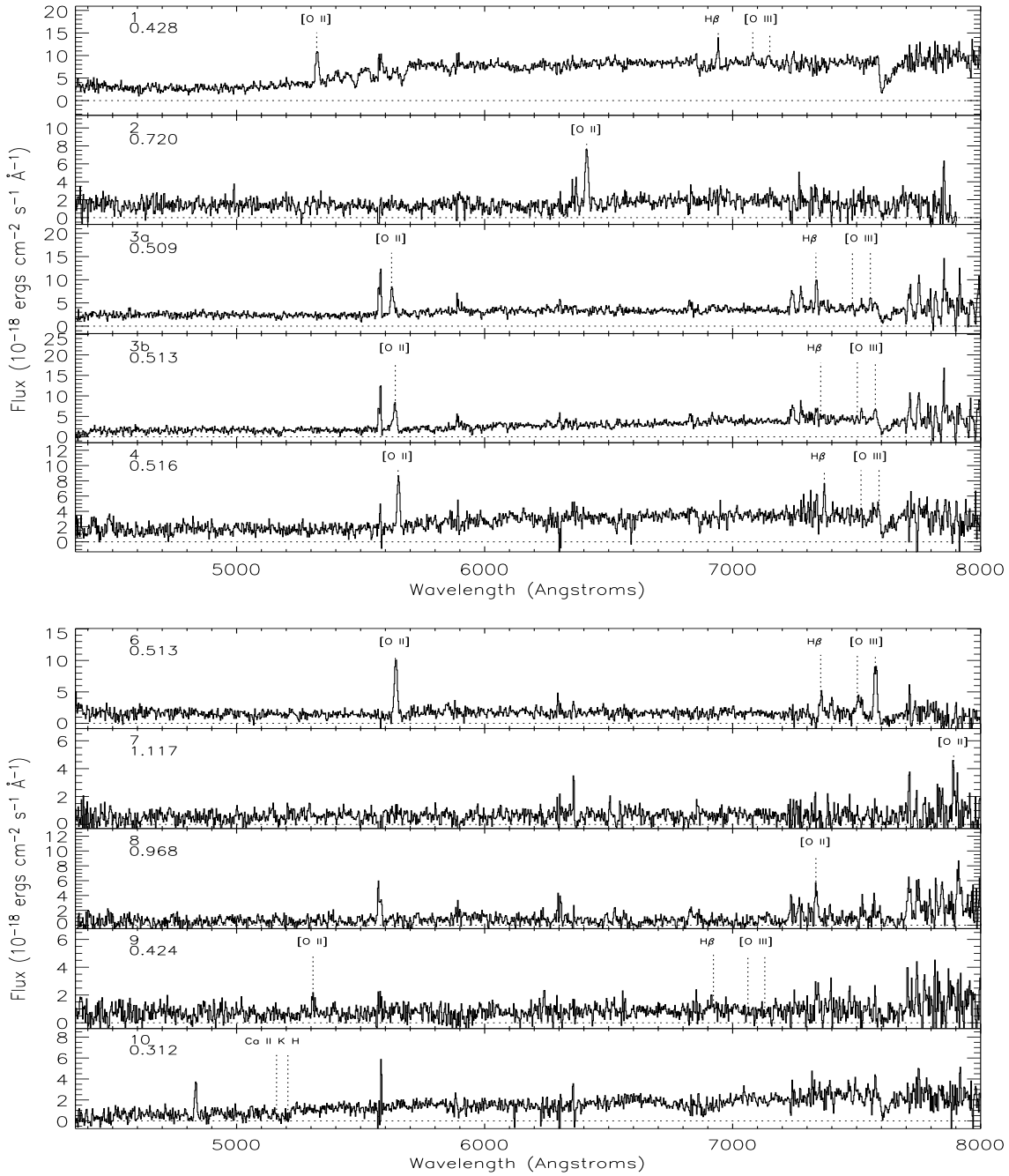


Fig. 1a. Spectra of galaxies observed in the HDFs. The ordinate gives the flux (in $\text{erg cm}^{-2} \text{s}^{-1} \text{\AA}^{-1}$). The wavelength coverage extends between 4200\AA and 8200\AA . The numbers on the top left corner of the spectra correspond to objects from Table 2 while the second number denotes the redshift. Note that for objects 1–39 the resolution is $\Delta\lambda/\lambda \sim 440$ while for objects 40 to 94 resolution is $\Delta\lambda/\lambda \sim 260$ (due to different grism filter combination). Since the wavelength coverage is common we present both spectra together.

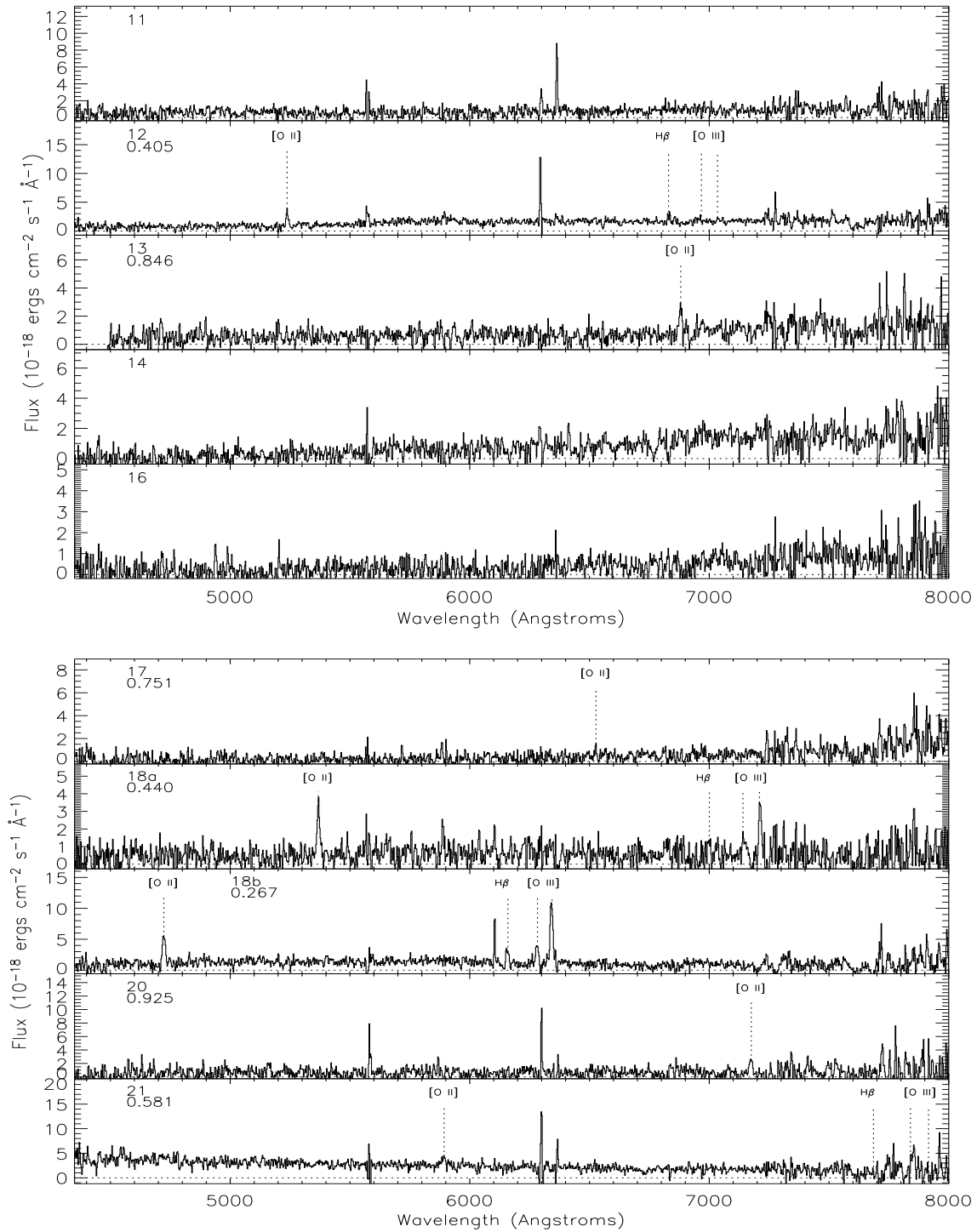


Fig. 1b. cont.

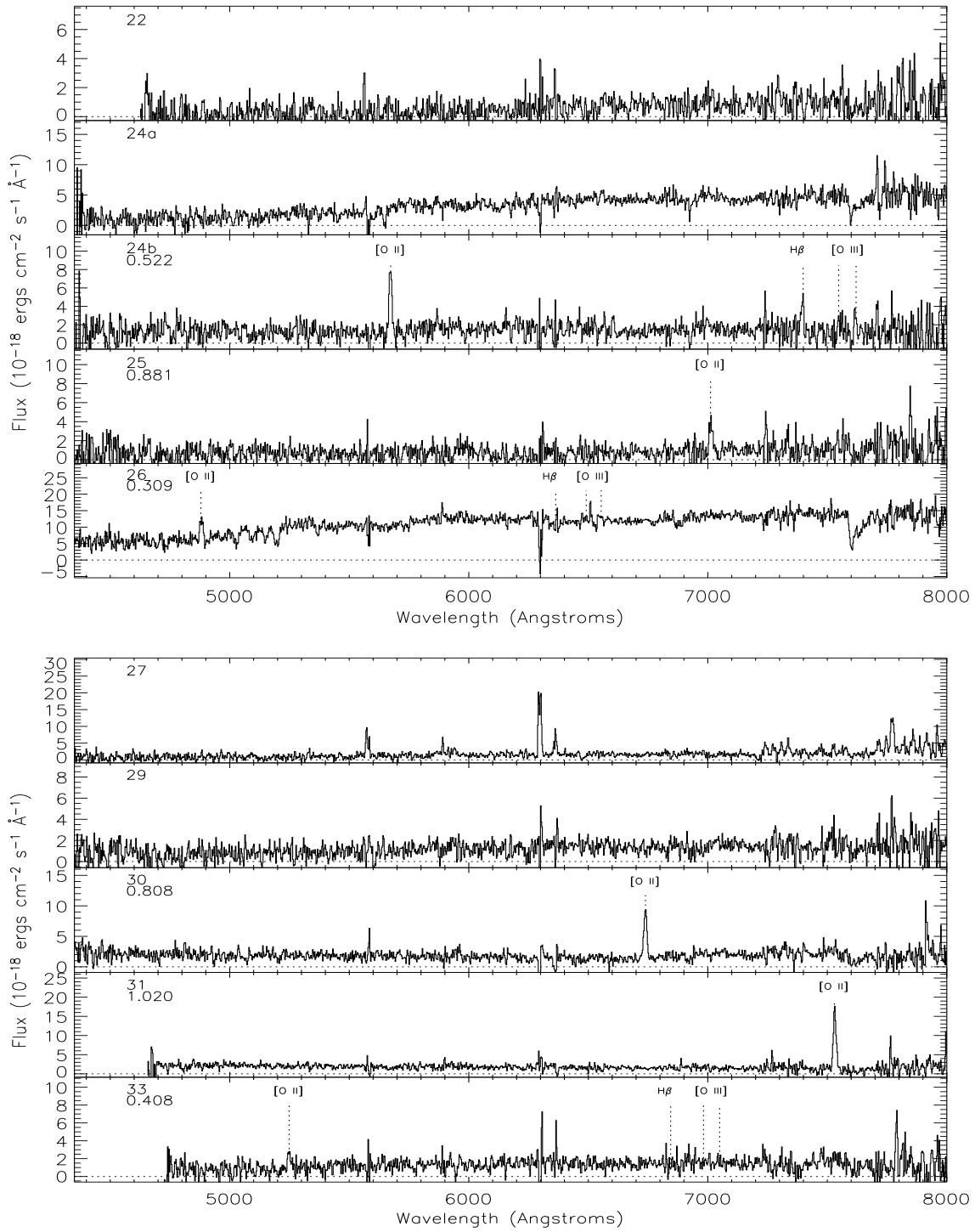


Fig. 1c. cont.

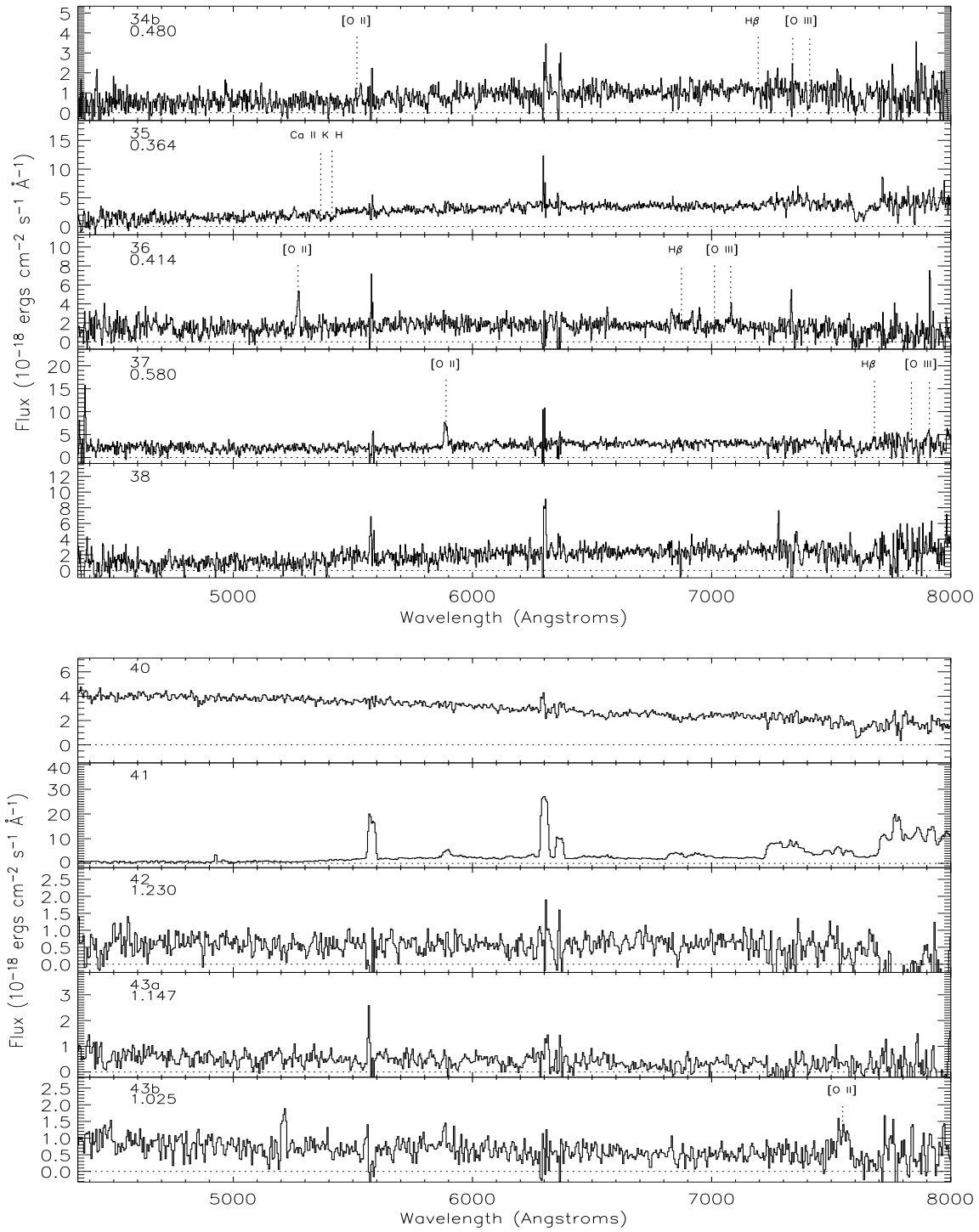


Fig. 1d. cont.

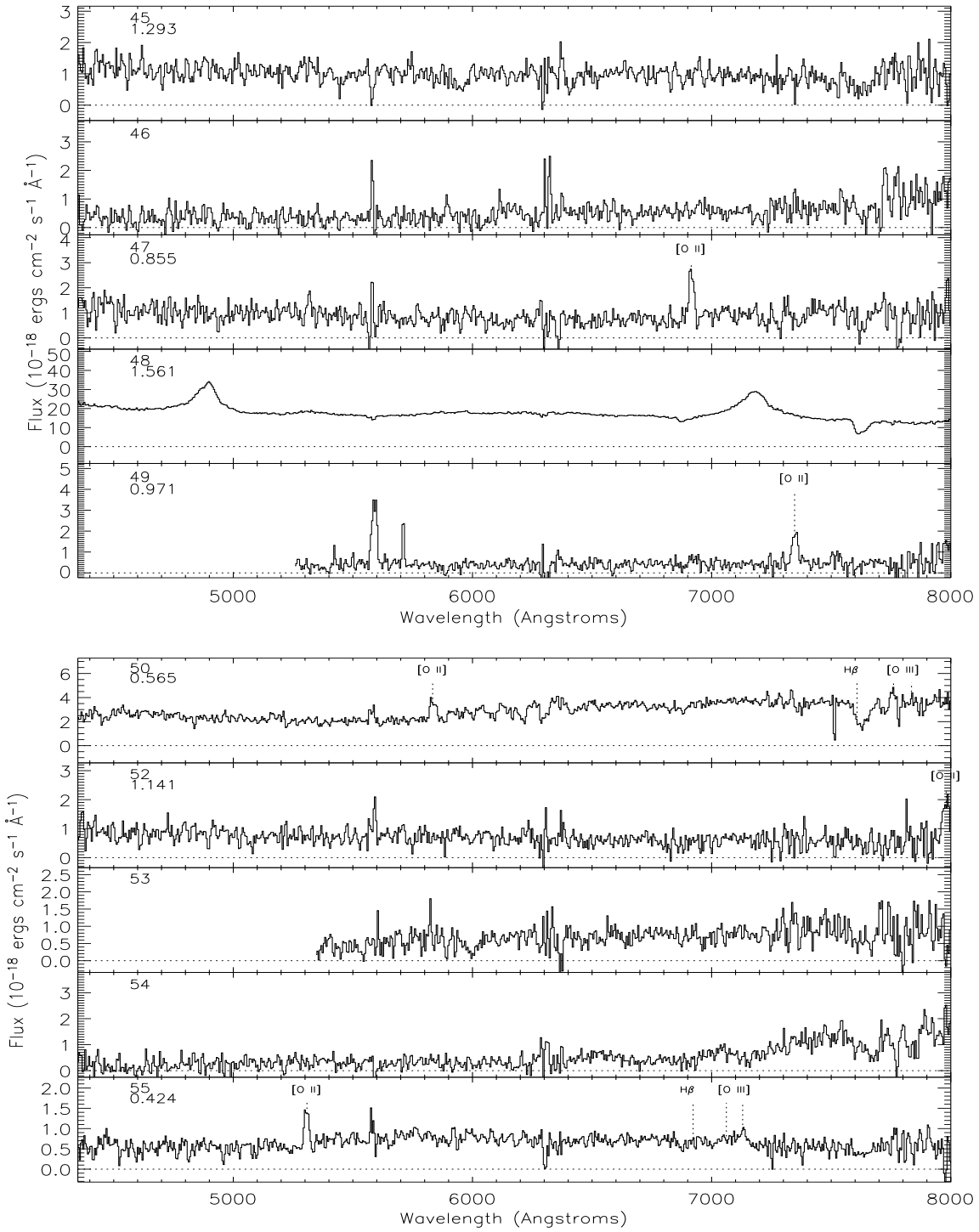


Fig. 1e. cont.

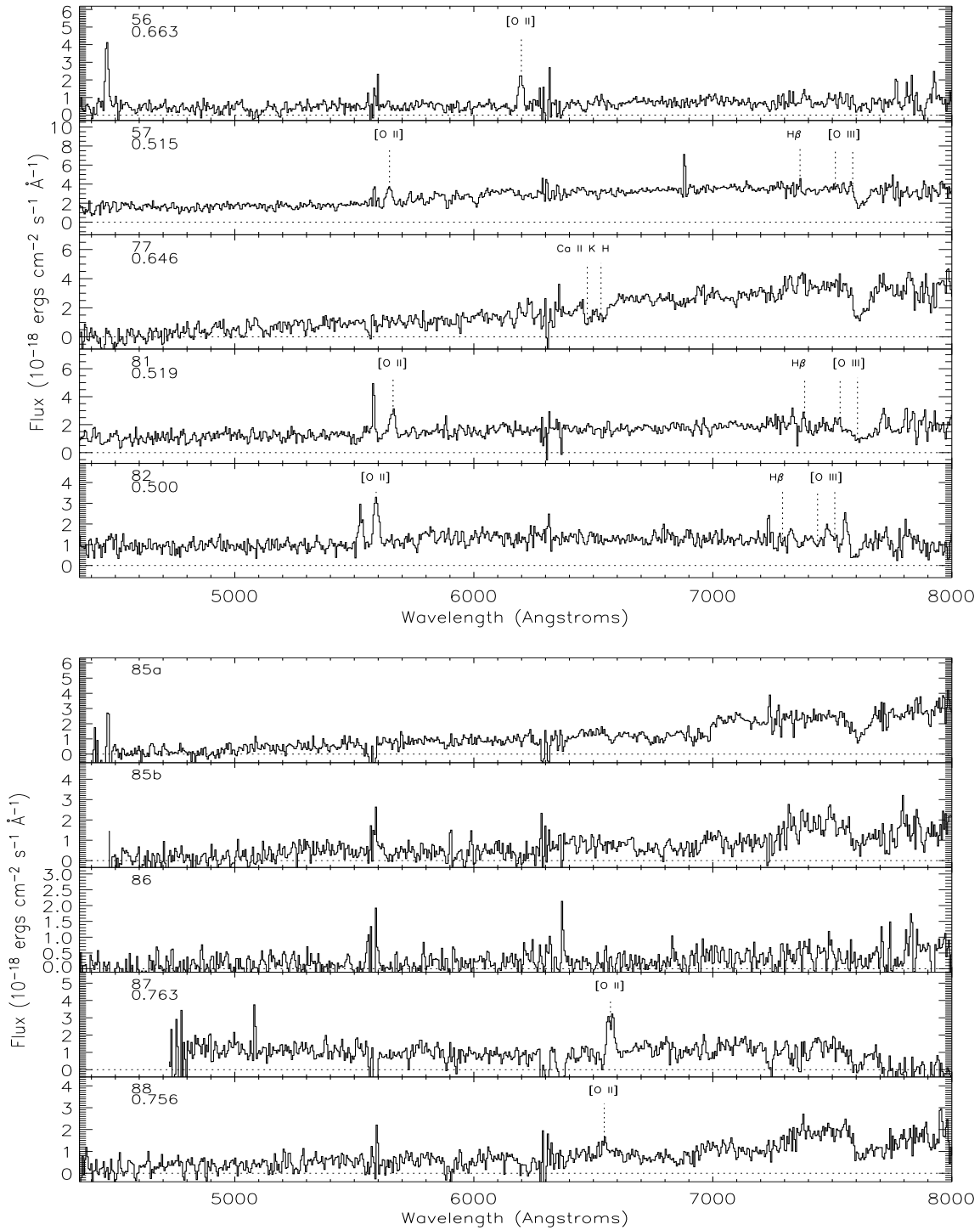


Fig. 1f. cont.

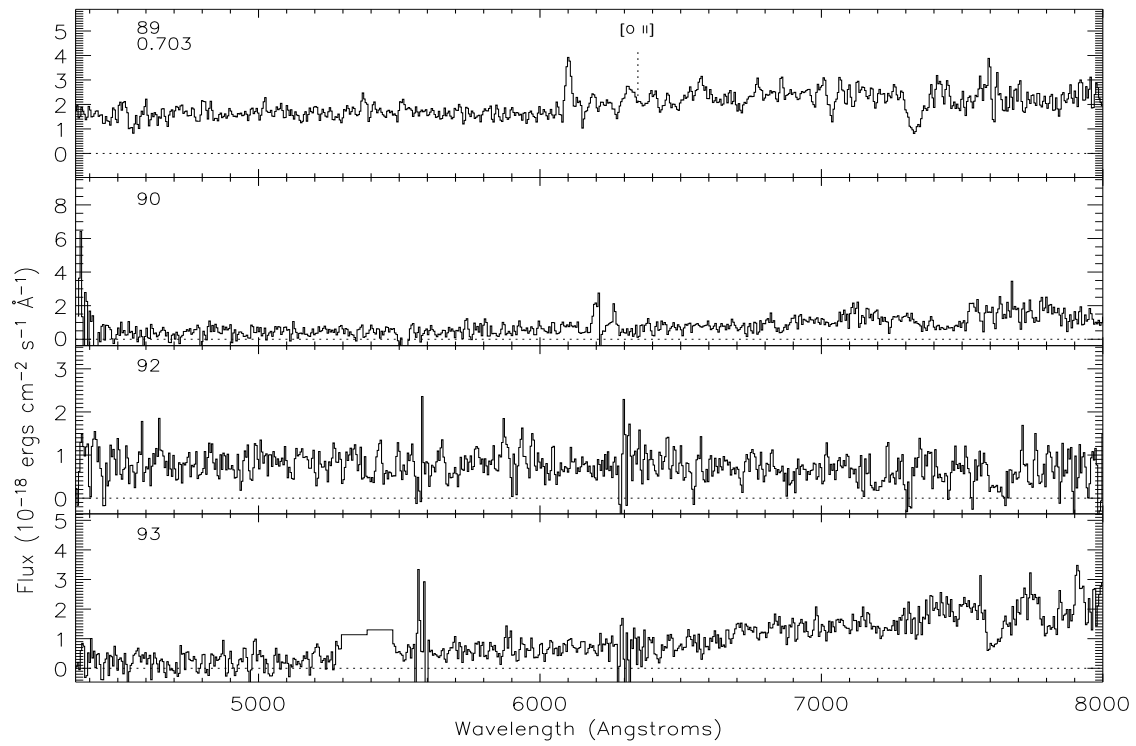


Fig. 1g. cont.

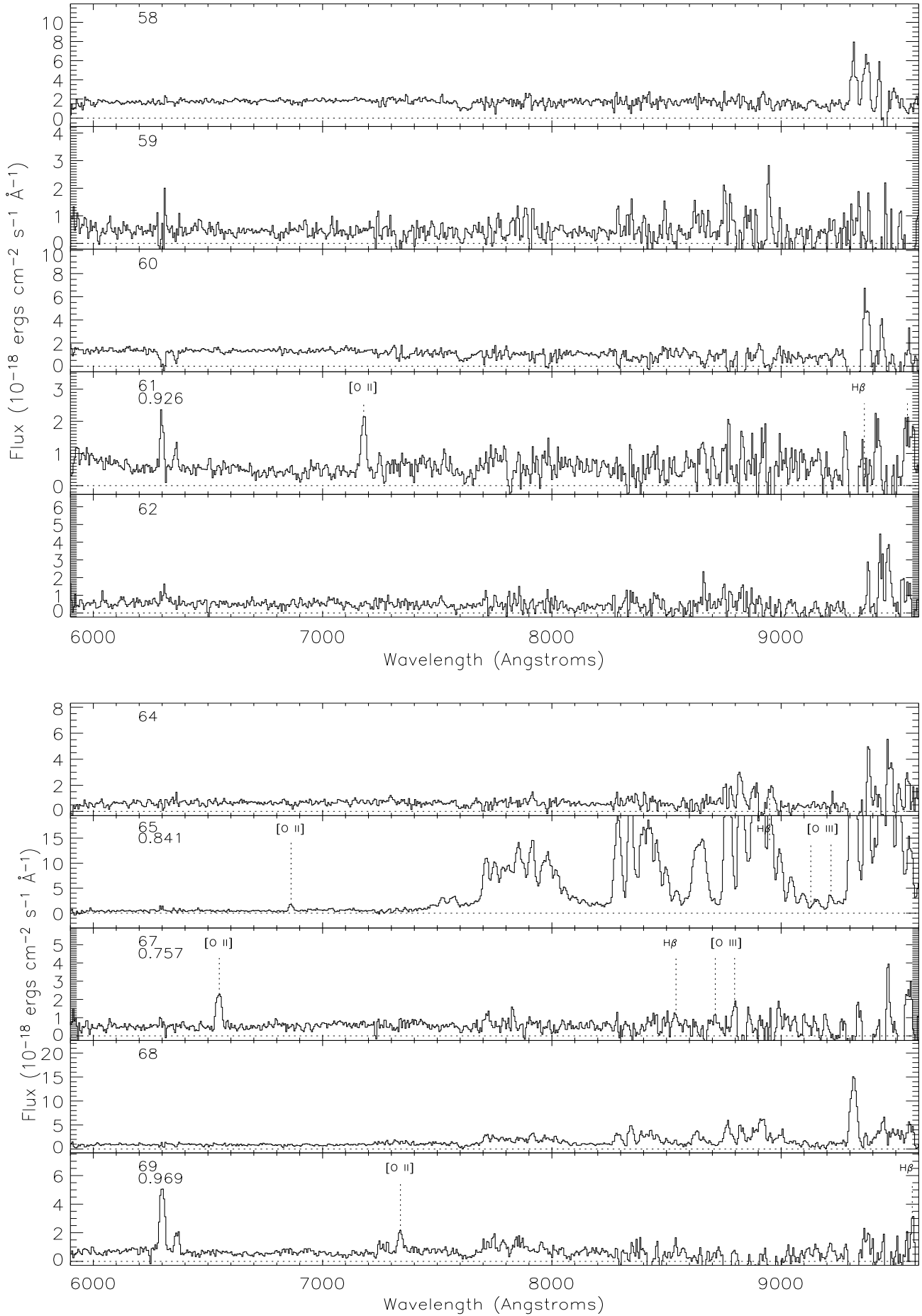


Fig. 2a. Same as Figure 1. The wavelength coverage extends between 6000 – 9200Å

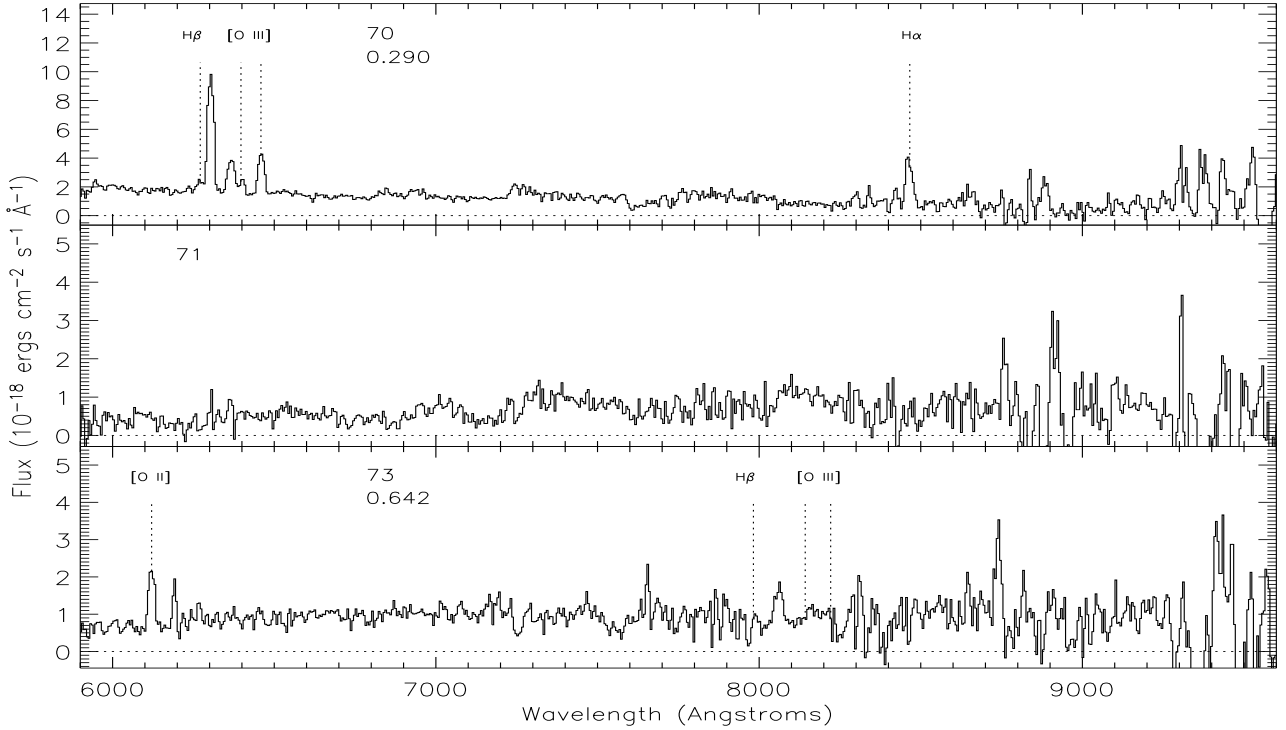


Fig. 2b. cont.

To estimate SFR for the current sample of HDFS galaxies we use the relationship given by Kennicutt (1998) assuming a Salpeter IMF ($0.1\text{--}100 M_{\odot}$), a constant star formation scenario and solar abundances:

$$SFR(M_{\odot}/\text{yr}) = 1.4 \times 10^{-41} L([\text{OII}]) (\text{erg s}^{-1}) \quad (2)$$

$[\text{OII}]\lambda 3727$ luminosities were calculated from the measured $[\text{OII}]\lambda 3727$ fluxes and the measured redshifts. We applied aperture correction factors (with average value of 1.3) to account for the light missed by our $1.2''$ slit. We calculated aperture corrections in two different ways: (1) we smoothed the WFPC2 F814 image to a resolution of $1.2''$ (to simulate the seeing during the present observations) and then measured the ratio between the total object counts (in the image) and the object counts through an artificial $1.2''$ slit; (2) for each galaxy we estimated the continuum flux at 3727\AA from the V_{AB} magnitude (recall that for $z\sim 0.6$ the V band filter samples the rest-frame UV light) and calculated the $[\text{OII}]\lambda 3727$ flux from the Equivalent Width (EW, $[\text{OII}]\lambda 3727$) measured from our spectra. Both methods lead to similar correction factors of ~ 1.3 .

However, because the observed $[\text{OII}]\lambda 3727$ line flux is extremely sensitive to extinction, an estimate of extinction should be made before we calculate SFRs. We base our extinction estimates on the comparison between predicted and observed $V-K$ colour index (magnitudes taken from Table 2). We use the Starburst99 code (Leitherer et al. 1999) for various star formation histories (i.e., bursts of different durations and ages, and continuous star formation) and calculate the range of intrinsic colours. The

intrinsic $V-K$ colours predicted by the models are in the range 1.1 – 1.5. We apply infrared (Poggianti 1997) and optical (Coleman 1980) K-corrections for spiral (Sc) galaxies (assuming the median redshift of our sample $z\sim 0.6$). Comparing the observed $V-K$ colours of our galaxies **with** the predicted ones we obtain a median extinction A_V of 0.9 assuming a screen model for the extinction (we assume no extinction in the K-band). This corresponds to an upwards correction factor of 3.5 in the $[\text{OII}]\lambda 3727$ line fluxes. We list the final aperture-corrected and extinction-corrected individual SFRs in Table 3.

5. $[\text{OII}]\lambda 3727$ Luminosity function and global SFR density

5.1. $[\text{OII}]\lambda 3727$ Luminosity Function

A direct estimate of the present-day SFR activity in the Universe can be obtained by constructing the $[\text{OII}]\lambda 3727$ luminosity function (LF) from the present sample galaxies. We used the V/V_{max} method (e.g. Felten 1977) to estimate the number density of galaxies in the various luminosity bins. In computing V_{max} however, we have to take into account that the sample is incomplete especially towards the fainter magnitude bins. Given the completeness function (Eqn 1) estimated in Section 3.2 the appropriate formula for each galaxy's volume V_{max} is:

$$V_{max} = \int \eta_i \frac{d^2 V_z}{d\Omega dz} \Delta\Omega dz \quad (3)$$

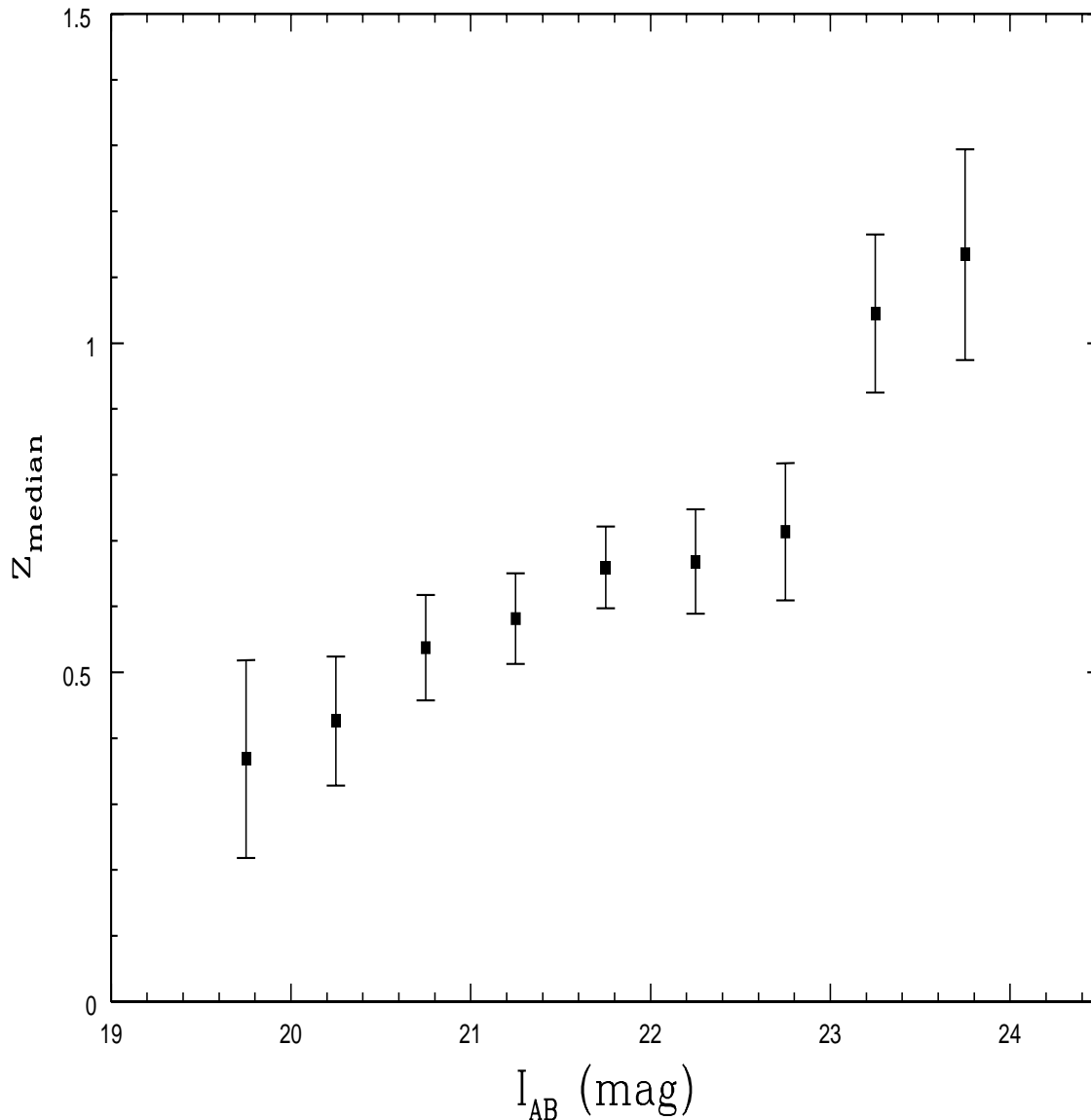


Fig. 3. Median redshift as a function of I_{AB} .

In the V/V_{max} method the luminosity density is obtained from:

$$\phi(L)\Delta(L) = \sum_i \frac{1}{V_{max}(L_i)} \quad (4)$$

where V_{max} is the maximum volume over which a galaxy is observable given the survey's apparent luminosity and the selection criteria. The sum includes all galaxies in the luminosity interval $L_i \pm 0.5\Delta L$. The errors are obtained assuming a Gaussian distribution which may not be very realistic for bins at the bright and faint ends where statistics are rather poor.

The LF constructed according to the V_{max} method is shown in Fig. 5. We then fit the LF with a Schechter (1976) function, and the best-fitting parameters (for a limiting [OII] λ 3727 flux of 1.02×10^{-17} erg cm $^{-2}$ s $^{-1}$) are: $\alpha = -1.24 \pm 0.12$, $\phi^* = 10^{-2.56 \pm 0.08}$ Mpc $^{-3}$, $L^* = 10^{42.33 \pm 0.07}$

erg s $^{-1}$. The solid line in Fig. 5 represents the Schechter function for the LF.

Since the luminosity function is well fitted by a Schechter function with $\alpha \leq -2$, $\phi(L)$ can be integrated over the whole range of luminosities :

$$L_{tot} = \int L\phi(L)dL = \phi^* L^* \Gamma(2 + \alpha) \quad (5)$$

For the observed luminosities the *total* [OII] λ 3727 luminosity density is $L_{[OII]} = 10^{39.42 \pm 0.05}$ erg s $^{-1}$ Mpc $^{-3}$ (for $0.5 < z < 1.5$, $\langle z \rangle = 0.8$). We note that for a Schechter function the luminosity density is dominated by L_* galaxies, so galaxies outside the observed luminosity range do not introduce large errors as long as galaxies near L_* are included and the faint end slope is $\alpha \leq -2$ (e.g. Tresse et al. 2001). A similar result for the *total* luminosity density is obtained by summing up $L[OII]/V_{max}$ for each galaxy.

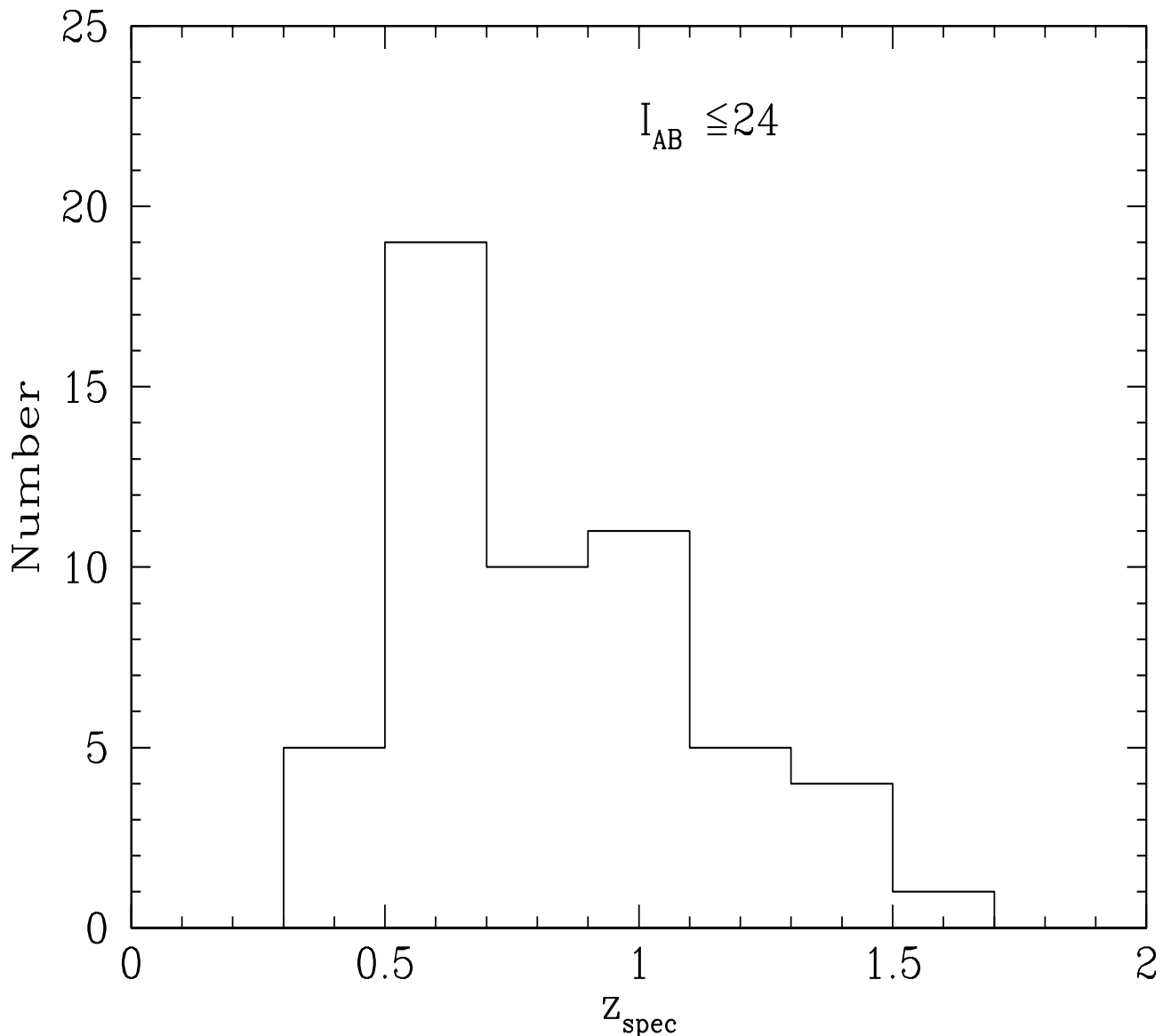


Fig. 4. Redshift distribution for all objects with confirmed spectroscopic redshifts.

This gives the directly observed luminosity density $L_{[\text{OII}]}$ $= 10^{39.12} \text{ erg s}^{-1} \text{ Mpc}^{-3}$.

In addition to the total $[\text{OII}]\lambda 3727$ luminosity density estimate we divided our sample into three redshift bins at $\langle z \rangle = 0.4$ and $\langle z \rangle = 0.8$ and $\langle z \rangle = 1.2$, while for each individual bin we estimated the $[\text{OII}]\lambda 3727$ luminosity density. For each individual bin we used the sum of the individual densities for each galaxy (as described above) to find: $10^{38.40 \pm 0.19} \text{ erg s}^{-1} \text{ Mpc}^{-3}$ at $\langle z \rangle = 0.4$, $10^{38.70 \pm 0.14} \text{ erg s}^{-1} \text{ Mpc}^{-3}$ at $\langle z \rangle = 0.8$, and $10^{38.90 \pm 0.22} \text{ erg s}^{-1} \text{ Mpc}^{-3}$ at $\langle z \rangle = 1.2$. The $[\text{OII}]$ luminosity density as a function of median redshift is shown in Figure 6. Although these later estimates suffer from small number statistics (in each bin we have $10 < n < 20$ galaxies), we note an evident trend towards higher luminosity density with increasing redshift over the range $0.4 < z < 1.2$.

5.2. Global SFR density

Using Equation (2) we can transform $L_{[\text{OII}]\lambda 3727}$ into a *global* SFR density. The total $[\text{OII}]\lambda 3727$ luminosity density we estimated in 5.1 translates into an SFR density of $0.015 \pm 0.03 \text{ M}_{\odot} \text{ yr}^{-1} \text{ Mpc}^{-3}$. If we assume a median extinction of $A_V = 0.9$ (see Section 4) then the total extinction-corrected $[\text{OII}]\lambda 3727$ luminosity density translates into SFR density of $0.11 \pm 0.02 \text{ M}_{\odot} \text{ yr}^{-1} \text{ Mpc}^{-3}$.

In Figure 7 we plot SFR densities vs. redshifts from the present spectroscopic survey (for the redshift range 0.4–1.2) supplemented with data from other surveys in the literature. We restricted ourselves to SFR estimates based on $[\text{OII}]\lambda 3727$ surveys in order to avoid conversions from H_{α} to $[\text{OII}]\lambda 3727$ luminosities. For the local Universe we used the SFR estimated by Gallego et al. (2002), and Hammer et al., (1997) for redshifts between

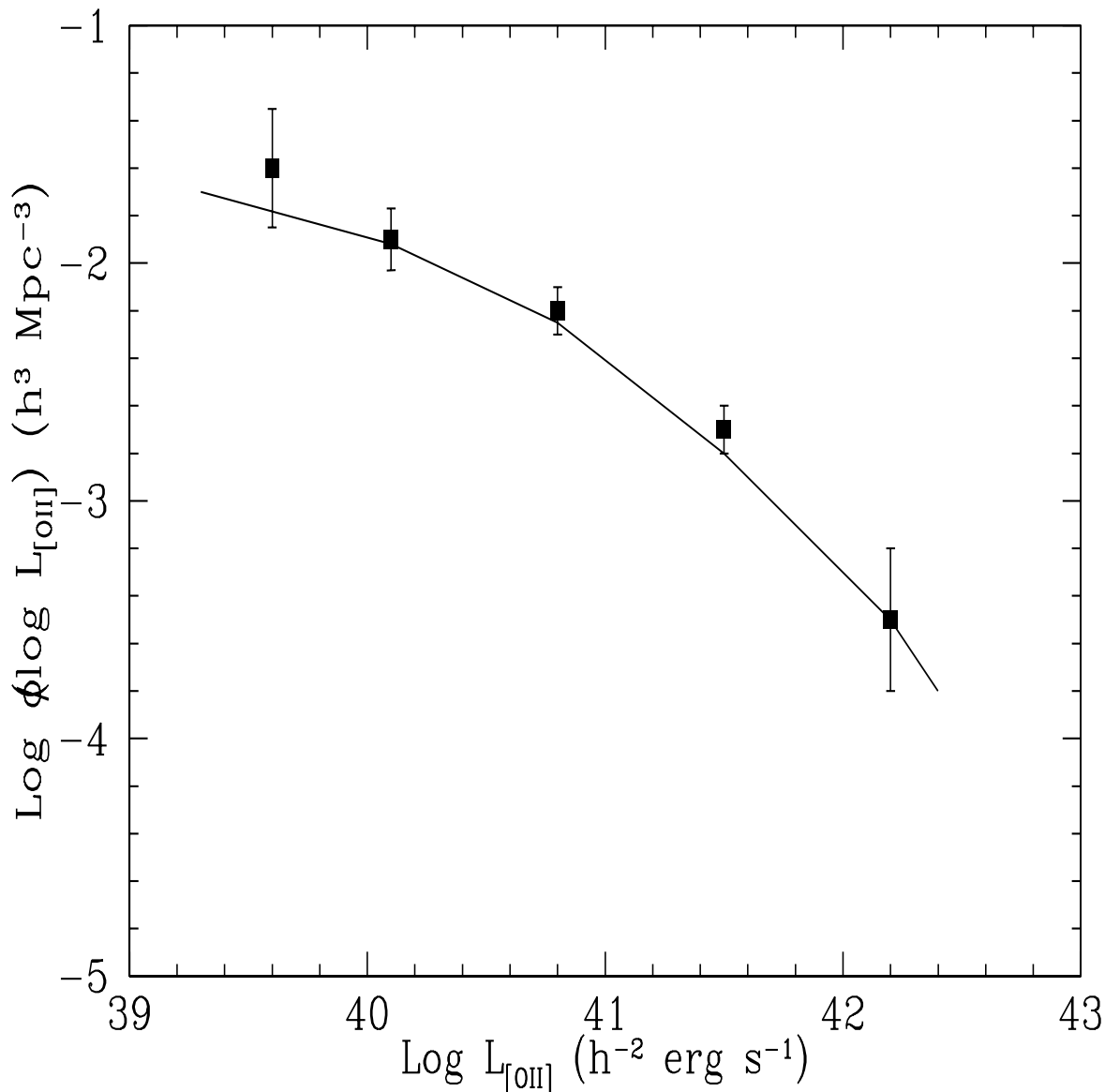


Fig. 5. [OII] luminosity function based on the V_{max} method with no extinction-corrections applied.

0.5 and 1.0. For redshifts beyond $z \simeq 1.5$ we used the results from Vanzella et al. (2002) and Steidel et al. (1997). Our results are in good agreement with the Canada-France-Redshift-Survey (CFRS, Hammer et al., 1997) results for the same redshift range. Unfortunately, most surveys provide only the observed luminosities and not the extinction corrected values. For the present data we plot both observed and extinction-corrected values.

Our present data show evidence for strong evolution from the local Universe out to $z \simeq 1.2$. Such a strong evolution of the SFR has also been observed with the H_α survey of Tresse et al. (2002) and the CFRS (Hammer et al. 1997). Assuming that the evolution of the SFR density with redshift follows a relationship of the $(1+z)^n$ form, then the combination of all the SFR data points implies a value for $n \simeq 4$. We caution, though, that this result is

to some degree dependent on the local SFR density value used. As an example the local Universe SFR density value derived from the H_α survey of Singleton et al. (2001) is lower than the value of Gallego et al. (1995). Irrespective of the local value, however, our present data show a clear rise in the SFR density by a factor of 6 in the $0.4 < z < 1.2$ regime.

6. Conclusions

We have presented new spectroscopic redshifts for 50 galaxies in the HDFs and Flanking Fields. We determined redshifts based on the detections of several emission lines such as [OII] $\lambda 3727$, H_β and [OIII] $\lambda 5007$ and the absorption features CaII H, K $\lambda \lambda 3968.5$ and 3933.7 \AA .

The redshift range of the present galaxy sample is $0.6 < z < 1.2$ with a median redshift of 1.13 (at $I \simeq 23.5$ not

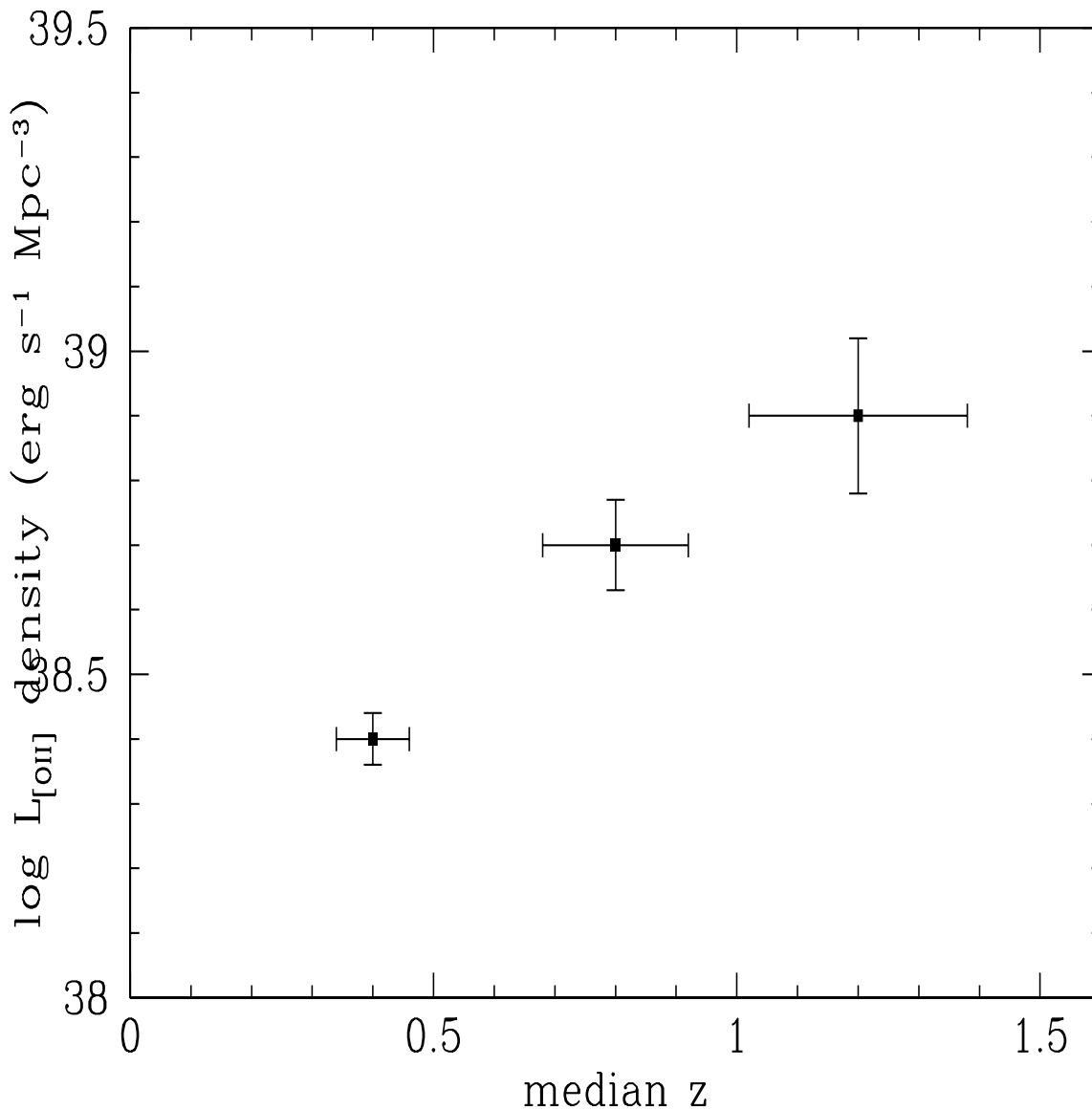


Fig. 6. [OII] luminosity density as a function of median redshift.

corrected for completeness). A large fraction of the galaxies detected are starbursts while the remaining $\sim 10\%$ are ellipticals. The *individual* star formation rates have been estimated for the emission line objects and the extinction correction rates range between $0.5\text{--}30 M_{\odot}/\text{yr}$. Based on the present data we have estimated the *global* SFR density of the Universe out to $z\sim 1.3$ and found it to be $0.11\pm 0.02 M_{\odot} \text{ yr}^{-1} \text{ Mpc}^{-3}$ using the total extinction corrected [OII] $\lambda 3727$ luminosity density.

Our data show evidence of a strong evolution from the local ($z=0$) Universe out to $z\sim 1.3$, following $(1+z)^4$. Finally, the availability of 8m class telescopes allows us to sample the evolution of the $z\approx 1$ Universe precisely and improve on previous determinations.

Acknowledgements. We acknowledge support of the EU TMR Network “Probing the Origin of the Extragalactic

Background Radiation” (HPRN-CT-2000-00138). We thank Michel Denefeld and his team for acquiring the data and Niranjana Thatte for help with data analysis. SB thanks MPE for the hospitality during his visits.

References

- Appenzeller, I., Bender, R., Boehnhardt, H., et al. 2000, ESO Messenger, 100, 44
- Arnouts, S., Moscardini, L., Vanzella, E., et al. 2002, MNRAS 329, 355
- Bergeron, J., Petitjean, P., Cristiani, S., et al. 1999, A&A343, 40
- Casertano, S., et al. 2000, AJ, 120, 2747
- Cohen, J.G., Hogg, D.W., Blandford, R., et al. 2000, ApJ538, 29

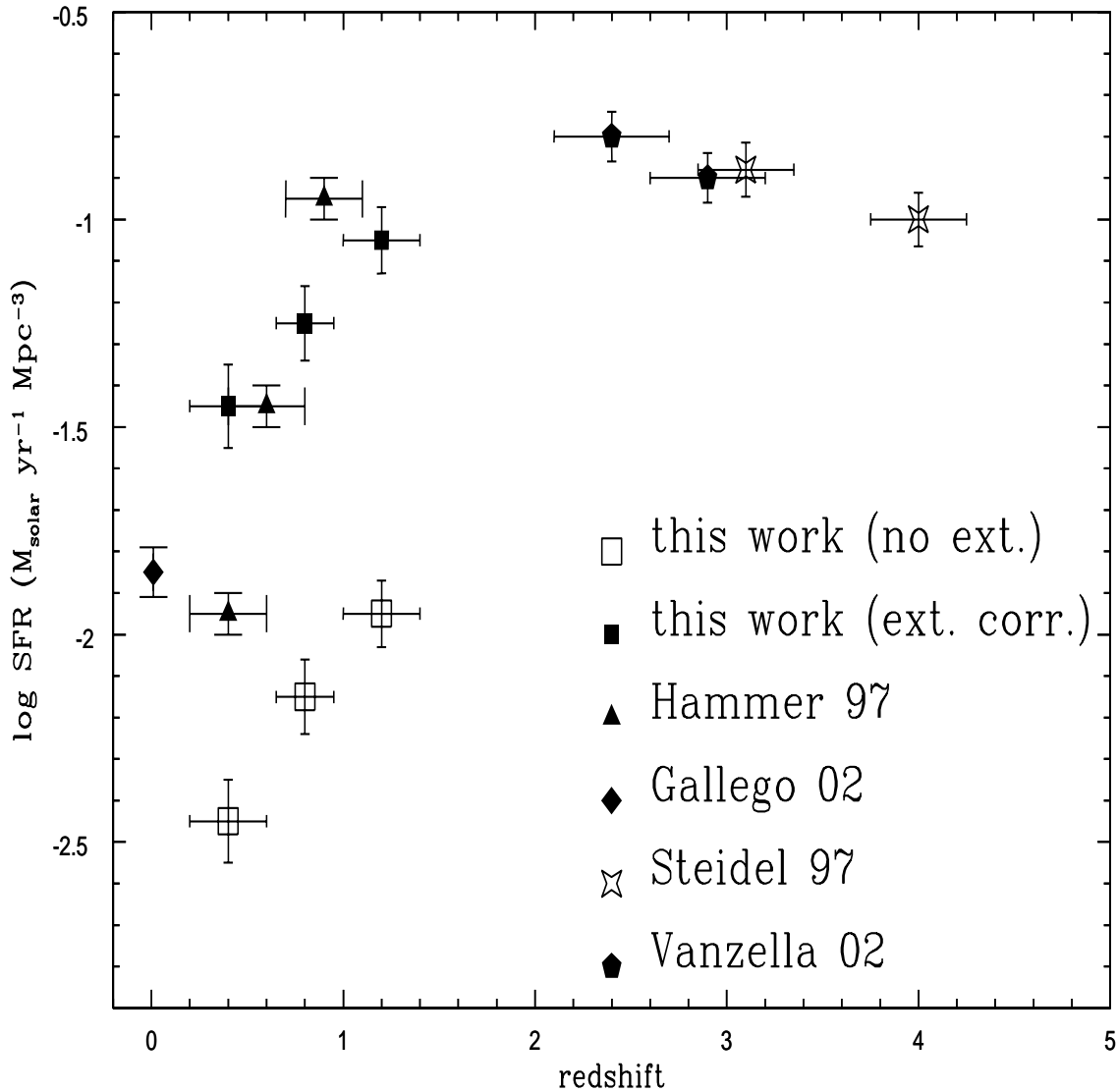


Fig. 7. SFR densities based on the present data, supplemented with literature values. Both the observed and extinction-corrected values are shown for the present sample and are represented as open and filled squares. Filled diamonds correspond to Gallego et al. (2002); filled triangles are for Hammer et al. (1997), filled pentagons for Vanzella et al. (2002) and filled stars are for Steidel et al. (1997).

Coleman, G.D., Wu, C.-C., Weedman, D.W. 1980, ApJ43, 393
 Cristiani, S., Appenzeller, I., Arnouts, S., et al. 2000, A&A, 359, 489
 Da Costa, L., et al. 1998, A&A submitted, astro-ph/9812105
 Felten, J.E., 1977, AJ82, 861
 Franceschini, A., Berta, S., Rigopoulou, D., et al. 2003, A&A, 403, 501
 Gallego, J., Zamorano, J., Aragon-Salamanca, A., Rego, M. 1995, ApJLett 455, 1
 Gallego, J., Garcia-Dabo, C.E., Zamorano, J., Aragon-Salamanca, A., Rego, M. 2002, ApJLett, 570, 1

Hammer, F., Flores, H., Lilly, S.J., 1997, ApJ481, 49
 Kennicutt, R.C., 1998, ARAA, 36, 189
 Leitherer, C., et al., 1999, ApJS, 123, 3
 Mann, R.G., Oliver, S., Carballo, R., et al. 2002, MNRAS, 332, 549
 Oliver, S., Mann, R.G., Carballo, R., et al. 2002, MNRAS, 332, 536
 Page, M.J., & Carrera, F.J., 2000, MNRAS, 311, 433
 Poggianti, B. M. 1997, AAS, 122, 399
 Rigopoulou, D., et al. 2000, ApJ, 537, L85
 Rudnick, G., et al. 2001, AJ, 122, 2205
 Saracco, P., Giallongo, E., Cristiani, S., D'Odorico, S., Fontana, A., Iovino, A., Poli, F., & Vanzella, E. 2001,

- A&A, 375, 1
Sawicki, M., & Mallen-Ornellas, G., 2003, AJ, 126, 1208
Schechter, P., 1976, ApJ203, 297
Singleton, C., 2001, PhD thesis, Univ. Nottingham
Teplitz, H. I., Hill, R. S., Malumuth, E. M., Collins, N. R., Gardner, J. P., Palunas, P., & Woodgate, B. E. 2001, ApJ, 548, 127
Tresse, L., Dennefeld, M., Petitjean, P., Cristiani, S., White, S., et al. 1999, A&A346, 21
Vanzella, E., Cristiani, S., Saracco, P., Arnouts, S., et al. 2001, AJ, 122, 2190
Vanzella, E., Cristiani, S., Arnouts, S., et al. 2002, A&A, 396, 847
Williams, R. E., et al. 2000, AJ, 120, 2735

Table 2. The data

No	RA(J2000)	Dec(J2000)	ID ¹	U _{AB}	B _{AB}	V _{AB}	R _{AB}	I _{AB}	J _{AB}	H _{AB}	K _{AB}	HST ID ²	ISO ID ³
1	22 33 04.90	-60 30 30.7	BTC35585	22.03	21.33	20.59	20.10	19.60					
2	22 32 46.35	-60 30 47.3											
3 ⁴	22 32 55.65	-60 31 16.9	EIS746	23.23	22.69	21.83	21.16	20.51	20.06	19.59	19.33		49
4	22 32 54.82	-60 31 31.1	EIS707	24.97	24.16	23.36	21.73	21.30	20.63	20.10	19.93		45
5	22 33 06.40	-60 31 47.0	STAR										
6	22 32 58.83	-60 32 18.5	EIS983	23.97	23.69	23.61	23.04	22.87	22.76	22.42	22.54		
7	22 32 53.35	-60 32 39.1	EIS621	24.85	24.49	24.20	23.66	23.21	22.05	21.50	21.30	720	41
8	22 33 03.85	-60 33 08.6	EIS1130	25.19	25.08	24.81	24.35	23.70	23.01	22.78	22.58	1236	
9	22 32 53.05	-60 33 28.4	EIS605	25.14	24.63	24.45	23.84	23.21	21.49	20.95	20.82	1539	
10	22 32 47.61	-60 33 47.2	EIS337	27.15	25.34	23.82	22.87	22.22	21.52	21.37	21.85	1922	
11	22 32 48.94	-60 34 04.6	EIS404	24.96	24.68	24.57	23.79	23.40	21.65	21.38	21.32	2285	
12	22 32 59.53	-60 34 37.7	EIS933	25.63	24.78	23.91	23.18	22.70	21.84	21.31	20.65		56
13	22 33 06.97	-60 34 51.4	BTC29103	25.97	25.22	24.71	23.67	22.77				W3-254	71
14	22 32 59.86	-60 35 18.5	EIS950	26.17	25.65	23.42	22.39	21.43	20.40	19.90	19.58		
15	22 32 53.11	-60 35 39.0	EIS608	27.48	25.87	25.55	24.93	23.68	22.25	21.67	21.53	W6-41	38
16	22 32 52.77	-60 36 02.6	BTC27181	26.30	26.64	25.53	23.61	22.44				W6-71	
17	22 32 59.19	-60 36 19.4	BTC26849	24.53	24.04	23.55	22.90	21.84				W5-286	
18 ⁴	22 32 47.44	-60 36 43.8	BTC26367	24.03	23.39	22.79	22.61	22.41					
19	22 33 00.23	-60 37 03.0	BTC26054	23.05	22.92	22.49	22.04	20.97				W6-225	
20	22 33 38.67	-60 33 10.2	EIS1022	24.10	23.86	23.57	23.25	22.50					
21	22 33 36.73	-60 33 43.1	BTC31064	22.99	22.50	22.34	22.38	21.80					
22	22 33 33.01	-60 34 28.1	BTC29784	26.14	26.09	24.28	23.47	22.51				W4-365	
23	22 33 31.43	-60 32 53.4	BTC32445	25.32	25.00	23.33	22.45	21.51					
24	22 33 26.93	-60 34 10.2	BTC30872	23.98	23.53	22.92	22.27	21.98				W4-307	
25	22 33 24.24	-60 33 28.2	BTC31402	24.11	24.11	23.74	23.15	22.34				W4-164	
26	22 33 21.23	-60 33 32.5	BTC31436	22.98	22.00	20.84	20.25	19.68				W4-173	
27	22 33 17.09	-60 32 37.3											
28	22 33 16.04	-60 31 28.2	BTC34392	24.05	23.21	22.11	21.28	20.64					
29	22 33 12.20	-60 34 00.9	BTC30516	24.72	24.48	23.30	22.55	21.77				W3-118	
30	22 33 09.43	-60 33 44.2	BTC30918	23.38	22.97	22.74	22.57	21.79				W3-76	
31	22 33 06.43	-60 34 34.7	BTC29684	22.95	22.63	22.22	22.20	21.58				W3-206	
32	22 33 01.85	-60 33 16.6	EIS1041	24.21	23.67	23.13	22.49	22.26	21.80	21.49	21.34	1285	
33	22 32 59.47	-60 34 38.0	EIS933	25.63	24.78	23.91	23.18	22.70	21.84	21.31	20.65	W5-27	
34	22 32 57.12	-60 31 52.7	EIS819	24.92	24.24	23.58	22.71	22.26	21.59	21.24	21.10	134	
35	22 32 53.91	-60 33 13.6	EIS659	25.08	23.66	22.21	21.50	21.11	20.63	20.39	20.26	1237	
36	22 32 50.28	-60 32 03.9	EIS469	23.43	23.18	22.63	22.24	21.98	21.52	21.69	21.23	254	
37	22 32 47.59	-60 34 08.6	EIS336	23.20	22.82	22.33	21.71	21.29	20.80	20.36	20.24	2338	28
38	22 32 45.34	-60 33 32.6	25.24	23.87	EIS213	22.70	21.99	21.52	20.83	20.56	20.36	1646	
39	22 33 10.28	-60 33 01.3	STAR										
40	22 33 07.21	-60 32 39.2	BTC32860	23.26	22.60	22.21	22.07	22.32					
41	22 33 05.36	-60 33 21.7	EIS1199	26.12	25.41	25.15	24.79	24.17	23.39	22.48	22.33	1440	
42	22 33 01.64	-60 34 13.7	EIS1024	25.16	25.07	24.99	24.62	23.48	23.66	23.34	23.15	2438	60
43 ⁴	22 32 58.67	-60 34 46.8	EIS891	24.58	24.42	24.55	24.08	23.42	22.72	22.53	22.41	W5-43	
44	22 32 55.53	-60 35 07.4	EIS744	24.97	24.49	24.47	23.95	23.68	22.56	21.92	21.89	W5-91	
45	22 32 52.08	-60 33 24.2	EIS557	24.32	23.90	24.01	23.61	23.44	22.57	22.32	22.17	1484	
46	22 32 49.73	-60 34 13.6	EIS451	25.88	25.30	25.18	24.47	23.57	22.21	21.80	21.46	2461	
47	22 32 45.74	-60 32 51.1	EIS238	24.26	24.04	24.10	23.67	23.17	22.74	22.65	22.70	919	
48	22 32 43.42	-60 33 51.7	EIS114	20.51	20.11	20.23	20.01	19.85	19.78	19.42	19.53		19

Table 2—Continued

No	RA(J2000)	Dec(J2000)	ID ¹	U _{AB}	B _{AB}	V _{AB}	R _{AB}	I _{AB}	J _{AB}	H _{AB}	K _{AB}	HST ID ²	ISO ID ³
49	22 32 39.27	-60 35 31.0											
50	22 32 35.95	-60 32 31.4											
51	22 32 32.82	-60 35 22.4	BTC28273	24.38	23.99	23.53	23.35	22.78					
52	22 32 30.33	-60 34 48.4	BTC67954	23.93	23.92	23.46	23.15	22.10					
53	22 32 27.41	-60 35 37.7	BTC27871	26.01	24.65	24.16	23.68	22.84					
54	22 32 24.76	-60 34 13.5	BTC30054	–	25.71	25.13	24.05	22.68					
55	22 32 20.93	-60 31 55.6	BTC33644	24.22	23.89	23.13	22.76	22.25					
56	22 32 19.14	-60 34 50.3	BTC29075	25.32	24.70	24.60	23.35	23.04					
57	22 32 16.42	-60 32 34.1	BTC32922	24.09	23.26	22.54	21.78	21.16					
58	22 32 50.33	-60 30 36.0	BTC35349	25.43	24.01	22.72	22.28	21.78					
59	22 32 56.03	-60 31 01.7	BTC69318	24.31	23.49	22.89	22.49	21.55					50
60	22 32 50.82	-60 31 22.0	BTC34349	25.27	23.57	22.80	22.50	22.02					34
61	22 32 30.52	-60 31 37.2	BTC69165	23.36	23.42	23.14	22.12	20.47					
62	22 32 56.69	-60 32 12.2	EIS780	26.74	26.08	25.97	26.08	25.55	24.16	23.30	23.54	390	
63	22 32 55.86	-60 32 20.4	EIS772	24.29	24.06	23.92	23.37	23.22	23.05	22.97	23.07	474	
64	22 32 49.07	-60 32 53.1	EIS422	24.78	24.52	24.24	23.55	23.16	22.77	22.59	22.50	960	
65	22 32 57.00	-60 33 05.1	EIS835	22.16	21.89	21.32	20.74	20.39	19.87	19.47	19.29	1091	
66	22 32 52.81	-60 33 28.1	EIS605	25.14	24.63	24.45	23.64	23.21	21.49	20.95	20.82	1621	
67	22 32 32.96	-60 33 55.4	BTC30682	24.06	23.58	22.70	21.97	20.91					
68	22 32 53.08	-60 34 12.6	EIS571	25.22	24.26	23.73	23.36	23.21	23.10	22.92	23.18	2465	
69	22 32 46.58	-60 34 38.4	EIS280	24.63	24.42	24.25	23.85	23.19	22.27	22.02	21.64		
70	22 32 37.29	-60 35 01.3	BTC28874	24.00	23.49	22.72	22.70	22.41				W2-346	
71	22 32 58.99	-60 35 30.8	EIS888		26.48	26.24	26.14		25.86				
72	22 32 56.70	-60 35 50.0	BTC27567	24.85	24.47	23.57	23.02	22.46				W5-208	
73	22 32 26.81	-60 36 12.8	BTC27012	24.70	24.27	23.60	22.76	22.24					
74	22 32 31.59	-60 36 29.4	BTC26697	22.98	22.33	21.42	20.12	20.71					
75	22 32 33.21	-60 36 58.2	BTC26262	23.13	22.32	21.11	20.36	19.85					
76	22 32 33.40	-60 37 16.5	BTC25736	24.77	23.48	22.22	21.28	20.61					
77	22 33 05.20	-60 30 59.7	BTC34928	–	24.04	22.78	21.70	20.58					
78	22 33 03.46	-60 31 15.0	EIS1114	25.24	24.74	24.85	24.78	23.57	23.07	22.43	22.01		67
79	22 32 57.60	-60 31 49.0	EIS838	25.58	25.27	25.19	24.66	23.82	21.79	21.17	21.15	W1-140	
80	22 32 53.70	-60 32 06.2	EIS645	26.19	25.91	25.43	24.68	23.64	22.48	21.92	21.62	306	43
81	22 32 57.76	-60 32 33.0	EIS847	24.18	23.75	23.34	22.61	22.29	21.79	21.39	21.35	627	
82	22 32 54.06	-60 32 51.6	EIS669	23.98	23.65	23.43	22.20	22.04	21.97	21.92	21.66	926	
83	22 33 03.85	-60 33 08.6	EIS1130	25.19	25.08	24.81	24.35	23.70	23.01	22.78	22.58	1236	
84	22 32 53.05	-60 33 28.4	EIS605	25.14	24.63	24.45	23.84	23.21	21.49	20.95	20.82	1539	39
85 ⁴	22 33 12.53	-60 34 03.5	BTC31360	24.12	23.83	22.07	20.71	19.82					84
86	22 33 00.50	-60 34 17.4	EIS986	26.88	27.76	26.10	24.95	23.48	22.63	22.22	22.12	2537	
87	22 33 14.23	-60 34 41.9	BTC29391	23.35	23.01	22.80	22.36	22.02					
88	22 33 10.09	-60 35 06.4	BTC28704	–	26.75	24.56	23.12	21.83				W3-343	
89	22 33 02.36	-60 35 25.3	EIS1053	23.01	22.64	22.29	21.80	21.23	20.94	20.67	20.60	W5-139	62
90	22 33 12.25	-60 35 45.4	BTC67521	25.46	25.44	24.34	18.51?	22.57				W5-139	
91	22 32 59.24	-60 36 19.2	BTC26849	24.53	24.04	23.55	22.90	21.84				W5-287	
92	22 32 58.29	-60 36 31.1	BTC26574	25.10	23.97	23.63	23.30	23.05				W5-345	
93	22 33 10.69	-60 37 05.2	BTC25937	26.39	24.93	23.68	22.48	21.18					
94	22 32 45.15	-60 37 17.1	BTC25547	25.57	26.09	24.61	23.70	22.51				W6-286	

¹the numbers correspond to identifications taken from (a) the BTC catalogue (see text) or (b) the ESO-EIS Deep catalogue (da Costa et al. 1998)

²ID taken from WFPC2 main catalogue (number corresponds to catalogue ID) or from WFPC2 flanking fields catalogue (ID number and field are reported)

³ID taken from ISO sources (Aussel et al. 2002, in prep)

⁴two galaxies in slit. Coordinates given from the original sample galaxy

Table 3. Spectroscopic Results

No	z^1	Descr. ²	[O II] $\times 10^{-17}$	H β erg cm ⁻² s ⁻¹	[O III]	SFR([O II]) M _⊙ / yr
1	0.428	em	10.971	5.855	3.726	6.819
2	0.720	em	9.730	-	-	21.246
3a3	0.509	em	8.863	-	0.285	8.595
3b	0.513	em	11.163	-	3.689	7.960
4	0.516	em	8.823	4.167	-	8.793
5	star	-	-	-	-	-
6	0.513	em	14.595	3.585	14.33	3.337
7	1.117	em	2.989	-	-	12.447
8	0.968	em	6.468	-	-	18.742
9	0.424	em	1.221	-	-	0.772
10	0.312	H+K	-	-	-	-
11	-	f.cont	-	-	-	-
12	0.405	em	3.007	-	-	1.723
13	0.846	em	2.865	-	-	9.073
14	-	cont	-	-	-	-
15	(1.39)	-	-	-	-	-
16	-	f.cont	-	-	-	-
17	0.751:	em	0.776	-	-	1.849
18a ³	0.440	em	4.507	-	3.876	3.110
18b	0.267	em	7.319	4.869	1.383	1.658
19	-	-	-	-	-	-
20	0.925	em	3.734	-	-	14.951
21	0.581	em	2.045	-	-	2.679
22	-	f.cont	-	-	-	-
23	-	-	-	-	-	-
24a	-	cont	-	-	-	-
24b	0.522	em	9.714	4.418	2.917	9.941
25	0.881	em	5.349	-	-	19.031
26	0.309	em	1.075	-	-	0.331
27	-	f.cont	-	-	-	-
28	-	-	-	-	-	-
29	-	f.cont	-	-	-	-
30	0.808	em	12.614	-	-	36.313
31	1.020	em	23.596	-	-	28.105
32	-	-	-	-	-	-
33	0.408	em	2.618	-	-	1.524

Table 3—Continued

No	z^1	Descr. ²	[O II] $\times 10^{-17}$	H β erg cm ⁻² s ⁻¹	[O III]	SFR([O II]) M _⊙ / yr
34a ³	star		-	-	-	-
34b	0.48:	em	1.3	-	-	1.156
35	0.364	H+K	-	-	-	
36	0.414	em	4.947	-	-	2.885
37	0.580	em	8.203	-	-	10.740
38	-	f.cont	-	-	-	-
39	star	-	-	-	-	-
40	-	f.cont	-	-	-	-
41	-	f.cont	-	-	-	-
42	(1.23)	-	-	-	-	-
43a ³	1.147	em	3.580			24.63
43b	1.025	em	4.405			23.02
44	-					
45	1.293	em	1.071	-	-	9.906
46	-	f.cont	-	-	-	-
47	0.855	em	5.002	-	-	16.531
48 ⁴	1.561	em	-	-	-	-
49	0.971	em	4.429	-	-	19.965
50	0.565	em	5.035	-	-	6.056
51	-	-	-	-	-	-
52	1.141	em	4.855	-	-	32.657
53	-	f.cont	-	-	-	-
54	-	cont	-	-	-	-
55	0.424	em	2.310	-	0.875	1.436
56	0.663	em	4.250	-	3.618	7.454
57	0.515	em	5.424	-	-	5.259
58	-	f.cont	-	-	-	-
59	-	f.cont	-	-	-	-
60	-	f.cont	-	-	-	-
61	0.926	em	4.472	-	-	17.681
62	-	f.cont	-	-	-	-
63	-	-	-	-	-	-
64	-	f.cont	-	-	-	-
65	0.841	em	2.946	-	-	9.311
66	-	-	-	-	-	-
67	0.757	em	5.542	-	-	13.344

Table 3—Continued

No	z^1	Descr. ²	[O II] $\times 10^{-17}$	H β erg cm ⁻²	[O III] s ⁻¹	SFR([O II]) M $_{\odot}$ / yr
68	-	f.cont	-	-	-	-
69	0.969	em	3.455	-	-	15.567
70 ⁵	0.290	em	-	1.933	1.703	-
71	-	f.cont	-	-	-	-
72	-	-	-	-	-	-
73	0.642	em	3.483	-	-	5.742
74	-	cont	-	-	-	-
75	-	-	-	-	-	-
76	-	-	-	-	-	-
77	0.646	H+K	-	-	-	-
78	-	-	-	-	-	-
79	-	-	-	-	-	-
80	(0.95)	-	-	-	-	-
81	0.519	em	4.385	-	-	4.445
82	0.505	em	6.599	-	2.432	6.117
83	-	-	-	-	-	-
84	(1.27)	-	-	-	-	-
85a ³	0.757	H+K	-	-	-	-
85b	-	cont	-	-	-	-
86	-	f.cont	-	-	-	-
87	0.763	em	7.638	-	-	18.972
88	0.756	em	1.210	-	-	3.008
89	0.734	em	5.866	-	-	12.786
90	-	f.cont	-	-	-	-
91	-	-	-	-	-	-
92	-	f.cont	-	-	-	-
93	-	cont	-	-	-	-
94	-	f.cont	-	-	-	-

¹redshift measured from emission or absorption lines

²Description of spectrum; em: emission lines detected, H+K: absorption features detected, cont: continuum detected but no lines, f.cont: faint continuum, no lines. A semicolon (;) symbol after a measured redshift denotes an uncertain redshift, a redshift within brackets refers to literature redshifts (from Rigopoulou et al., 2000 or Franceschini et al. (2003))

³two galaxies in slit

⁴This is a type I AGN (Franceschini et al. 2003). From the present observations we have detected CIV λ 1909 and MgII λ 2798 lines.

⁵The H $_{\beta}$ line is very close to a night-sky line. The quoted flux is a “de-blended” one. H $_{\alpha}$ has also been detected